Ultra Broadband Indoor Channel Measurements and Calibrated Ray Tracing Propagation Modeling at THz Frequencies

Sebastian Priebe, Marius Kannicht, Martin Jacob, and Thomas Kürner

Abstract: **Ultra broadband communication systems operated at THz frequencies will require the thorough knowledge of the propagation channel. Therefore, an extensive measurement campaign of 50 GHz wide indoor radio channels is presented for the frequencies between 275 and 325 GHz. Individual ray paths are resolved spatially according to angle of arrival and departure. A MIMO channel is recorded in a 2×2 configuration.**

An advanced frequency domain ray tracing approach is used to deterministically simulate the THz indoor propagation channel. The ray tracing results are validated with the measurement data. Moreover, the measurements are utilized for the calibration of the ray tracing algorithm. Resulting ray tracing accuracies are discussed.

Index Terms: **MIMO channel measurements, propagation modeling, ray tracing propagation simulations, THz communications, ultra broadband channel measurements**

I. INTRODUCTION

THz communication in the frequency range from 0.3 to 3 THz has evolved as a very good candidate to fulfill the exponentially growing need for wireless data transmission capacity [1]. Data rates up to 100 Gbit/s and beyond will foreseeably be required already within the current decade [2]. Prospective uses-cases are intra-chip communications, kiosk downloads, wireless private area networks and ultra fast wireless local area networks (WLANs) [3], [4]. A good overview over further applications in the THz band, such as imaging and material testing, can be found in [5].

Feasibility demonstrations of multi-Gbit/s links with mm and sub-mm waves [6], [7] have brought about industrial interest in the THz range for communications. Monolithic integrated circuits have been reported up to 670 GHz by Northrop Grumman as state of the art in 2011 [8]. Eventually, the Interest Group THz has been founded within the standardization framework of the IEEE [9].

As a prerequisite for the development and standardization of THz wireless LANs, optimum system concepts will have to be evaluated. Thorough knowledge of the THz indoor propagation channel is mandatory at that stage in order to account for realistic propagation conditions in the conception process. First

simple channel measurements of a point-to-point link on a desktop and a WLAN connection within a small office environment have been presented in [10] and [11]. In comparison with conventional WLAN carrier frequencies like 2.4 GHz, 5 GHz or even 60 GHz, arising differences and challenges are the high free space attenuation, the high reflection losses and the scattering from rough surfaces [12]. Furthermore, THz communications will have to cope with very high absolute bandwidths in the order of up to 50 GHz, highly dispersive materials [13] and a frequency-selective reflection behavior of multilayer materials [14]. A significant pulse form distortion could already be demonstrated in UWB channels due to dispersive propagation [15]. Thus, modeling approaches designed for any lower frequencies cannot by applied to the sub-mm wave range without significant modifications. Conventional single-frequency ray tracing (RT) [16] has been widely employed for the simulation of wireless propagation channels from the 1990s onwards [17]. RT has been extended to broadband frequency domain RT in order to correctly account for the huge employed bandwidths in our previous work [18]. Now, the conduction of THz channel measurements becomes indispensable for the validation of such a specific THz indoor propagation model.

The remaining paper is structured as follows. At first, Section II presents an extensive channel measurement campaign in an office scenario. A vector network analyzer (VNA) with frequency extensions mounted on rotation stages is used to record spatially resolved channel transfer functions (CTFs) with a bandwidth of 50 GHz from 275 to 325 GHz (Subsections II-A and II-B). Channel properties are evaluated in the temporal as well as in the spatial domain in the Subsections II-D through II-E including the polarization impact and the measurement accuracies. Additionally, 2×2 MIMO channel measurements are demonstrated in Subsection II-F.

In Section III, frequency domain RT is introduced to accurately predict the propagation behavior in indoor environments. The experimental data from Section II serves as a reference to validate the ray tracing propagation model. A novel RT calibration method is discussed in Subsection III-B. It is applied to significantly increase the prediction accuracy of the RT tool. Finally, calibrated RT predictions are compared to the measurements in Subsection III-C before the paper is concluded in Section IV.

II. THZ INDOOR RADIO CHANNEL MEASUREMENTS

THz radio channel measurements are essential for the correct propagation modeling. At such high frequencies, measurements

Fig. 1. Measurement setup.

Table 1. Measurement parameters.

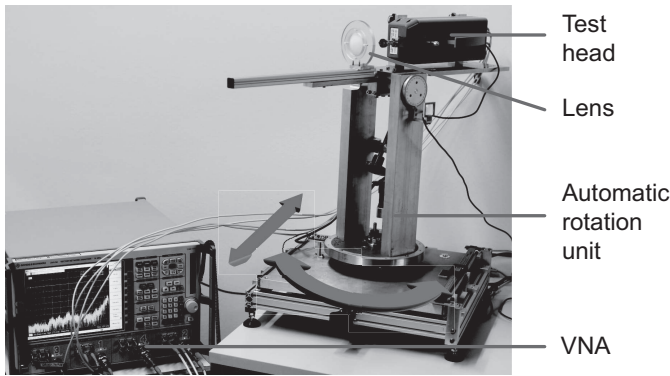| Symbol	Parameter	Value
f_{Start}	Start frequency	275 GHz
f_{Stop}	Stop frequency	325 GHz
B	Bandwidth	50 GHz
Δf_{IF}	Intermediate frequency bandwidth	10 kHz
N_f	Measurement points	3201
$\Delta \tau$	Temporal resolution	0.02 ns
τ_{max}	Maximum excess delay	64 ns
l_{max}	Maximum resolvable path length	19.2 m
HPBW_ϕ	Azimuth half power beamwidth	$\approx 2°$
$\Delta \phi$	Angular resolution	$2°$
PL_{max}	Maximum detectable path loss	145 dB

pose the versatile challenges that

- high path losses necessitate very high dynamic ranges
- huge bandwidths must be considered
- measurements must be recorded spatially resolved
- MIMO channels shall be characterized despite that omnidirectional antennas are not available.

These challenges will be addressed with direction-selective channel sounding in frequency domain and a virtual MIMO array.

A. Measurement Setup

The core component of the channel measurement setup is a Rohde & Schwarz ZVA50 vector network analyzer with frequency extensions ZVA-Z325, which generates a complex test signal between 220 and 325 GHz. The focus lies on the still unregulated spectrum from 275 GHz onwards [19], so that the VNA is operated from 275 GHz up to its maximum frequency of 325 GHz. This allows for channel measurements with a total bandwidth of $B = 50$ GHz in the lower THz range of interest. In previous work, comparable measurements were limited to $B = 10$ GHz [11]. A channel bandwidth of 50 GHz corresponds to a very high temporal resolution of $\Delta \tau = 0.02$ ns. As a tradeoff between sweep time and maximum detectable path length l_{max}, the CTF is sampled at $N_f = 3201$ frequency points. 3201 points enable the resolution of a maximum excess delay $\tau_{\text{max}} = 64$ ns or $l_{\text{max}} = 19.2$ m. Another compromise is made between measurement time and noise level of the system. An IF filter bandwidth of $\Delta f_{\text{IF}} = 10$ kHz has been chosen. This allows for a dynamic range of about 65 dB at the waveguide outputs of the frequency extensions. A TRL calibration is applied to correct the measurements by the VNA system response. Remaining uncertainties after calibration amount to at maximum 1 dB [20].

A significant increase of the maximum detectable path loss is achieved with standard gain horns and focusing Polyethylene (PE) lenses at the TX as well as the RX unit. Their half power beamwidth (HPBW) amounts to approximately $2°$, with which an excellent spatial filtering and hence the distinct spatial resolution of individual multipath components (MPCs) can be achieved. The gains of the horn antennas and the PE lenses are determined according to the two antenna method [21]. This is repeated as a reference for every measurement in order to account for a potentially non-perfect placement of the lenses in front of the horns. Averaged over the entire frequency band and

multiple recorded references, the total antenna gain amounts to 80.1 dB. With the noise floor around $S_{21} = -65$dB, path losses of at maximum $PL_{\text{max}} = 145$ dB can be recorded. All parameters are summarized in Table 1.

Quasi-omnidirectional channel impulse responses (CIRs) are obtained by scanning the entire angular domain in the azimuth. For this purpose, the test heads are mounted on in-house-built rotation units driven by stepping motors, which are depicted in Fig. 1. The highly directive antennas can be turned against each other into any arbitrary direction in the azimuth. An angular resolution of $2°$ is chosen for the spatial sampling of the channel according to the antenna HPBW. A reference position switch guarantees repeatability and minimum angular deviations. Both test heads can be oriented vertically as well as horizontally, facilitating measurements in linear horizontal and vertical polarization.

MIMO channels can be measured by shifting the TX/RX units horizontally in the order of magnitude of one wavelength, i.e., 1 mm at 300 GHz (cf. Fig. 1). High mechanical shifting precisions below one wavelength are ensured through a worm drive and an electronic caliper. Quasi-omnidirectional CIRs are recorded consecutively at multiple, slightly different TX and RX positions. Next, the corresponding MIMO channels are be synthesized. That way, a virtual MIMO array is emulated.

Both, the VNA and the stepping motors are PC-controlled to automatically record the spatial measurements. With the parameters above, the duration of one complete omnidirectional SISO measurement in the azimuth, i.e., $360° \times 360°$, takes approximately 90 hours.

B. Spatially Resolved Channel Measurements

In view of THz wireless LANs, the channel measurements are conducted in a small office scenario depicted in Fig. 2. The transmitter emulates a WLAN access point and the receiver represents a nomadic device like a laptop on a desk. The dimensions amount to 3.59 m $\times$ 4.52 m $\times$ 2.82 m. All walls as well as the ceiling are coated with plaster and the floor is covered with carpet. The two glass windows are enframed with metal. Apart from the two wooden desks on which the rotation units are placed, the room is furnished with several wooden wardrobes. One of them is mounted elevated above the metal door.

Three different TX positions are considered at $TX_1 = (2.72$ m, 4.07 m, 1.38 m), $TX_2 = (0.5$ m, 4.02 m, 1.38 m), and $TX_3 = $
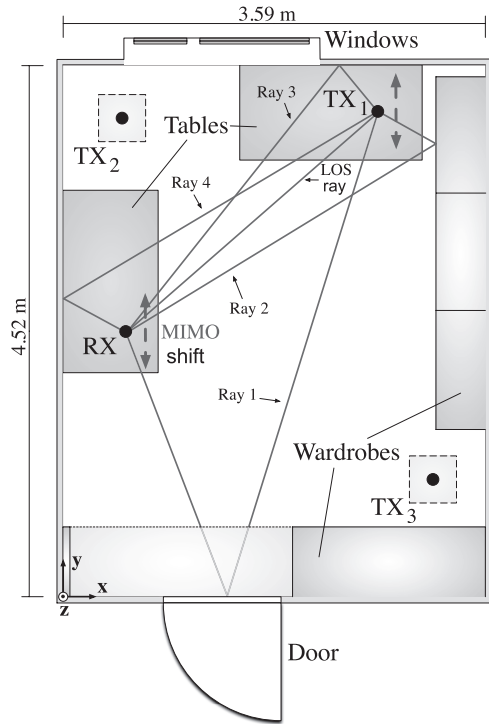
Fig. 2. Scheme of the investigated office scenario; true to scale.

Fig. 3. Measured angular power spectrum at TX position 1; reflection order of identified paths are indicated in italics.

(2.89 m, 1.12 m, 1.38 m), which correspond to typical placements of the access point in corners of the room. The RX remains on the desk at RX = (0.5 m, 2.2 m, 1.38 m) for each TX position. $180 \times 180 = 32{,}400$ CTFs are recorded over the entire angle of arrival/angle of departure (AoA/AoD) range of $360° \times 360°$ in order to synthesize the quasi-omnidirectional channel. Despite that the measurement setup would also permit a variation of the TX and RX elevation, the investigations are limited to the azimuth plane at a height of 1.38 m in order to significantly reduce the complexity of the measurements from 3D to 2D. The obtained results can qualitatively be transferred to measurements in other horizontal or in skewed planes. Only the varying polarization characteristics would have to be taken into account in case of different TX and RX heights.

Fig. 3 illustrates the path losses measured over the angles of arrival and departure. Both angles are given with respect to the x axis in mathematically positive direction. The path losses have been determined as the peaks of the power delay profiles (PDPs) recorded for the respective AoAs and AoDs. Due to the excellent spatial filtering, only one path is detected at maximum in every direction. The PDPs have been corrected by the antenna gain and the system impact. Note that the results presented in this paper always refer to linear θ polarization unless indicated otherwise. θ polarization, being equal to vertical polarization in the given setup, corresponds to TE reflections from the walls. Similarly, ϕ polarization equals horizontal polarization here. As TE reflections cause less reflection losses than TM reflections, more and higher order indirect paths can be detected in θ compared to ϕ polarization.

Multiple ray paths can be identified as distinct spots in the angular power profile. Interestingly, a certain spatial broadening of the supposedly discrete rays is observed. This is due to
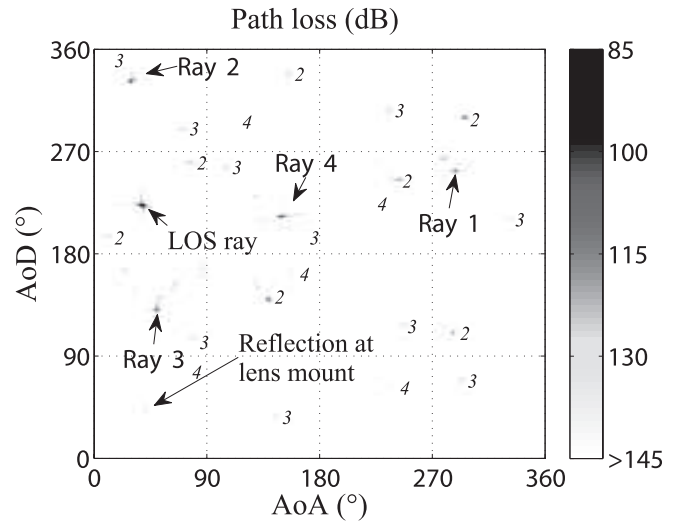
the horns antennas used to illuminate the PE lenses, which have a rather broad lobe with an HPBW of 17° [22]. They still receive a certain power that is radiated past the lenses even when they are turned out of the main path direction by a few degrees. Scattered rays, which may theoretically also broaden the pulses in the spatial domain [23], could not be detected separately in the power delay profiles and can be neglected as discussed later.

In contrast to a theoretical free space loss (FSL) of 91.2 dB at 300 GHz, the loss of the LOS ray extracted from the measured PDP amounts to 97.5 dB. The reasons for the deviation are fourfold. First, the channel frequency dispersion over the huge bandwidth as well as the impact of the inverse fast Fourier transformation (IFFT) cause a temporal pulse broadening. This effect occurs due to the frequency dependency of the free space attenuation and leads to a pulse distortion, which has already been observed for the LOS path in ultra wideband channels [15]. In consequence, the detected peak power is reduced by about 1.5 dB, *i.e.,* a higher PL is measured [18]. This is not respected in the theoretical discrete FSL for 300 GHz. Second, vertical antenna alignment has been optimized with a water level, but slightest misalignments can possibly not be avoided. Third, the channel is only sampled with a limited spatial resolution, which causes certain horizontal misalignment with respect to the actual AoAs/AoDs. Both misalignments affect the PL only marginally with typical deviations in the order of 1 dB as long as the rays are received well within the 3 dB HPBW. Fourth, the VNA calibration and the reference measurements bring about an inherent uncertainty (cf. the previous subjection).

The LOS ray as well as the four first order reflections have been marked in the profile and in the scenario scheme. All further rays detected above the noise level have been labeled with their reflection order in italics. For the identification of the rays, a geometric ray search according to the image source method [24] is employed. Based on vectorial scenario data, the engine searches for unobstructed, specularly reflected ray paths and determines their angles of arrival/departure as well as their reflection points up to an arbitrary order. In the second main

Table 2. Detected (Det.) vs. geometrically expected (Ex.) number of reflected paths.

Order	TX_1 Det.	TX_1 Ex.	TX_1, ϕ pol. Det.	TX_1, ϕ pol. Ex.	TX_2 Det.	TX_2 Ex.	TX_3 Det.	TX_3 Ex.
1st	4	4	4	4	2	4	4	4
2nd	7	7	7	7	4	6	7	7
3rd	10	10	6	10	5	8	8	8
4rd	5	11	1	11	1	10	3	8

part of the paper, this algorithm will be combined with an electromagnetic engine for complete ray tracing simulations.

Table 2 summarizes the number of paths resolved according to the reflection order that could be detected in contrast to the path number that is expected geometrically. Note that Table 2 respects the paths in the horizontal plane of the TX/RX units only and does not include reflections at the ceiling and/or the floor. At TX_1, all first through third order reflections as well as remarkable 5 out of 11 fourth order rays were recorded. Preliminary measurements in a similar scenario have been limited to up to the second order in our previous work [11]. Due to the higher reflection losses, only 6 out of 10 and 1 out of 11 rays were found above the noise level for the same TX position in ϕ polarization. For TX_2, the measurement equipment itself blocks several rays as the TX and RX units are aligned along the y axis. 2 first and 2 second order reflections could not be detected for this reason. At TX_3, all reflections up to third order have been found, whereas the wardrobe close to the transmitter position shadows several rays and reduces the number of expected third and fourth order rays by 2 and 3, respectively.

The angles determined from the geometric ray search could be fed into the spatial measurements as an a priori information in order to significantly speed up the scanning. Still, the entire angular range is considered in the measurements with the aim to potentially identify any rays scattered or diffracted at irregularities like the corners of the wardrobes. However, as can be seen in the angular power spectrum, no rays apart from the geometrically expected reflections could be detected. Any influence of the tables cannot be observed either for the reason of vertical spatial filtering. The only exception is a reflection at the lens mount of the TX for AoA and AoD $\approx 45°$, which is barely visible in the figure due to the high loss. This reflected ray is not part of the actual spatial channel but just occurs due to the measurement setup itself. It can be concluded that neither diffraction nor scattering remote from the immediate region around the specular reflection points plays any significant role. These results match the findings of previous dedicated scattering and diffraction measurements [12], [25].

C. Spatial and Temporal Measurement Accuracy

Apart from amplitude deviations, the measured AoAs/AoDs as well as the ToA may also differ from the geometrically expected ray characteristics. Impairments occur for two different reasons. First, the angular resolution is limited to 2° by the antenna HPBW, so that the actual AoAs/AoDs of the paths can inherently not be determined exactly with remaining deviations between -1° and 1°. Second, the accuracy of the geometrical calculations strongly depends on the precision of the input data like
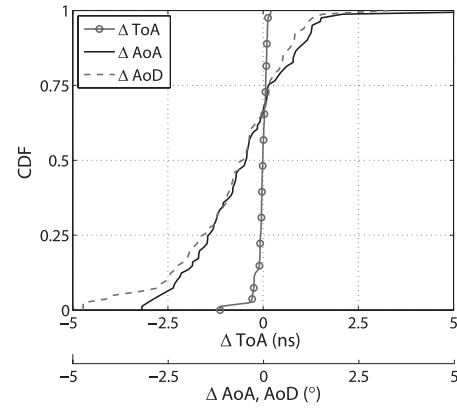

Fig. 4. Deviations between the geometrically expected and the measured AoAs, AoDs as well as ToAs for all TX positions.

Table 3. Mean absolute deviations between measured and geometrically expected path characteristics for different reflection orders.

	LOS	1st	2nd	3rd	4th
AoA	0.13°	1.20°	1.11°	1.03°	1.70°
AoD	0.13°	0.95°	1.06°	1.18°	2.04°
ToA	0.08 ns	0.06 ns	0.08 ns	0.08 ns	0.21 ns

the dimensions of the scenario and the positions of the TX/RX as well as those of the objects. Even slightest dimension inaccuracies cause slight ToA deviations in face of the very high temporal resolution of $\Delta\tau = 0.02$ ns, which corresponds to a resolvable distance of 6 mm.

In Fig. 4, the cumulative distribution functions (CDFs) of the spatial and temporal deviations between measurements and the geometrical modeling are depicted for all rays at the three TX positions. The delta is defined as $\Delta X = X_{\text{Geo}} - X_{\text{Meas}}$. More than 50% of the paths are measured within the inherent inaccuracy range ΔAoA,AoD $= [-1°, 1°]$ and almost 100% within $[-3°, 3°]$. Time of arrival differences are found between -0.1 and 0.1 ns for roughly 80% of the rays, *i.e.,* between -3 and 3 cm in terms of path lengths. Be aware that multiple reflections are included in the CDFs, for which position inaccuracies add up. The average inaccuracy per interaction is well below 3 cm.

Mean absolute deviations are summarized in Table 3 according to reflection order. As expected, the imprecisions increase with the number of reflections. Very low deviations around 1° and only 0.08 ns have been achieved for up to third order rays. The only limitation is the phase condition of all rays. Due to the remaining uncertainties compared to the very short wavelength, the phase can inherently not be predicted and reproduced exactly. Otherwise, dimension precisions down to the μm range would be required.

D. Broadband Channel Characteristics

Spatio-temporal channel properties become crucial for broadband system simulations including smart antennas. Fig. 5(a) illustrates the AoA/ToA profile for TX_1. Similar to the mere spatial domain, the antenna-induced broadening also affects the spatio-temporal properties. Still, all individual rays can be sep-
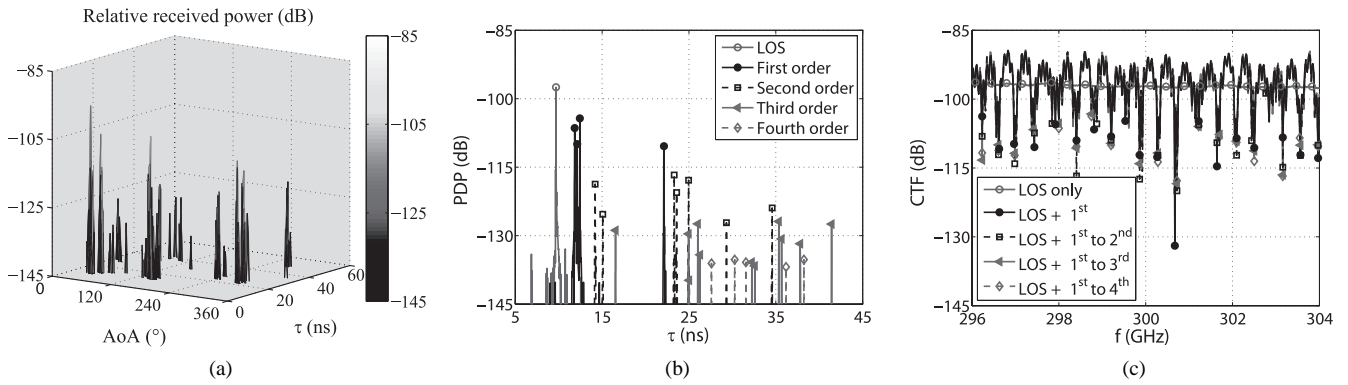
Fig. 5. Measured PDP and CTF in the office environment for TX position 1: (a) Measured AoA/ToA profile, (b) composed measured PDP resolved according to reflection orders, and (c) cut-out of the resulting CTF in consideration of different reflection orders.
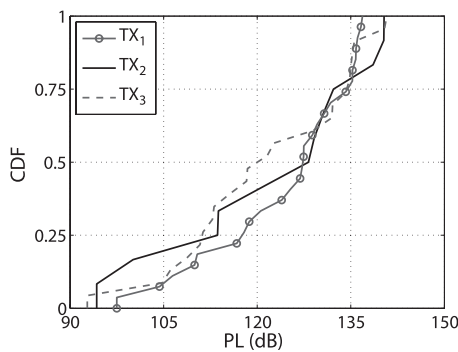

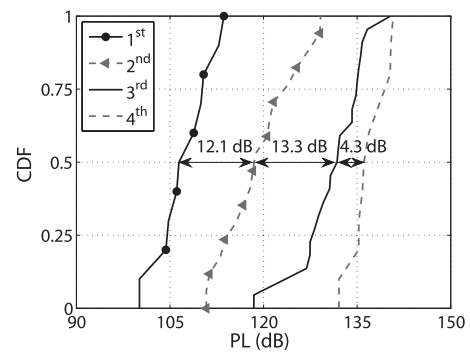Fig. 6. Ray path losses according to TX positions.

Fig. 7. Ray path losses according to reflection order over all TX positions.

arated. This will later be exploited for a ray mapping between measurements and ray tracing simulations during the RT calibration.

With the aim to evaluate the impact of the reflections on the broadband channel properties, Fig. 5(b) demonstrates the PDP for TX_1 resolved according to reflection order. Local maxima before and after the LOS peak do not correspond to rays, but are just a consequence of the noise introduced by the IFFT about 35 dB below the global maximum of the PDP.

The peaks of the two strongest first order reflections are attenuated by no more than 7 and 9 dB compared to the LOS. With increasing reflection order and increasing time of arrival, the ray amplitudes decrease, typically by 5 to 10 dB per reflection process. *E.g.*, second order reflections are found 18 dB and more below the LOS path. Accordingly, the LOS ray and the first order reflections also dominate the shape of the CTF as can be seen in Fig. 5(c). The displayed CTF has been cut out of the 50 GHz wide channel in order to clearly illustrate the fading behavior. For the measured LOS path, the CTF is almost flat over the depicted bandwidth of 8 GHz. A significant fading behavior is introduced when first order reflections are taken into account. Then, the CTF varies by 42 dB peak-to-peak. Second order rays cause a change of the amplitudes in the fading dips, but do not alter the general CTF shape. Third and fourth order reflections have hardly any further impact on the CTF. This can be seen with the help of the markers placed at the minima of the CTFs.

Allowing for a qualitative comparison between the three TX

positions, Fig. 6 depicts the CDFs of the occurring ray path losses for TX_1 through TX_3. Those range between 92 and 141 dB. Remarkably, all CDFs have a very similar function shape. In interpretation, this indicates similar multipath amplitudes and hence a very similar fading behavior for all measured TX positions. Obviously, the qualitative considerations from TX_1 above can also be transferred to TX_2 and TX_3 or even to further TX/RX constellations in the scenario.

Fig. 7 illustrates the ray path losses resolved according to reflection order. Again, the curves behave similarly and are just shifted towards higher losses for an increasing number of reflections. The fourth order curve differs slightly from the other graphs because of the incomplete number of detected fourth order rays. If all fourth order rays could have been measured, a similar graph like the other three curves would be expected.

For first order rays, the attenuations are higher by between 5.8 dB up to 19.3 dB compared to the LOS. The deviation between the least and the most attenuated ray increases from 13.5 dB for first order to 18.3 dB and 21.9 dB for second and third order rays, respectively. Mean attenuations of 107.7 dB, 119.6 dB, 131.3 dB, and 137.1 dB are determined. Excluding the additional attenuation caused by the longer path compared to the LOS, typical reflection losses are found between about 5 dB and 15 dB. The difference between the CDF curves shows that attenuations of 12–13 dB provide a good rule of thumb for the average additional losses per reflection to be expected in THz

Table 4. k-factor, RMS delay spread and AoA angular spread in the azimuth for the different TX positions and reflection orders.

	TX$_1$			TX$_1$, ϕ pol.			TX$_2$			TX$_3$		
	k	τ_{RMS}	σ_{AoA}	k	τ_{RMS}	σ_{AoA}	k	τ_{RMS}	σ_{AoA}	k	τ_{RMS}	σ_{AoA}
LOS only	-	0.27 ns	-	-	0.33 ns	-	-	0.63 ns	-	-	0.20 ns	-
LOS + 1st	1.69	2.88 ns	37.9°	4.63	3.17 ns	30.8°	1.90	1.63 ns	15.7°	6.34	1.86 ns	18.2°
LOS + 1st to 2nd	1.56	3.49 ns	39.8°	4.34	3.47 ns	31.9°	1.85	1.89 ns	16.6°	4.40	2.93 ns	26.4°
LOS + 1st to 3rd	1.54	3.69 ns	40.0°	4.33	3.55 ns	31.9°	1.85	1.99 ns	16.7°	4.33	2.99 ns	26.5°
LOS + 1st to 4th	1.53	3.72 ns	40.1°	4.33	3.55 ns	31.9°	1.85	1.99 ns	16.7°	4.32	3.01 ns	26.5°
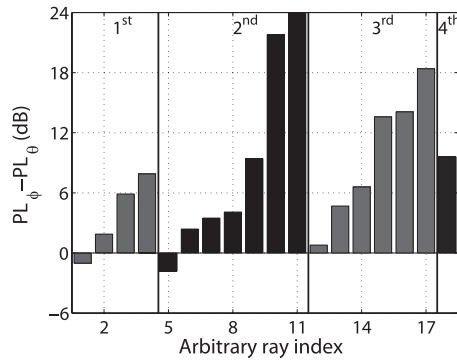
Fig. 8. Ray path loss differences between ϕ and θ polarization for TX$_1$ according to reflection order.

channels. This figure includes both the reflection loss as well as the higher free space attenuation due to the longer path.

Table 4 summarizes the k-factors, the RMS delay as well as the angular spreads for the different TX positions. The k-factor provides a measure for the multipath richness of a channel. It is defined as the ratio between the power of the strongest path divided by the power of all other rays. Rather low k occur at TX$_1$ and TX$_2$, indicating that the powers of the reflections are almost as high as the power of the LOS ray. Higher k-factors are observed in ϕ polarization at TX$_1$ for the reason that the reflections are attenuated more compared to θ polarization. Regardless of the position and polarization characteristics, third and fourth order reflections hardly influence the k-factor at all.

The RMS delay and the angular spread, which are calculated as the standard deviations of the power delay and the angular power profile, respectively, represent a measure for the temporal and the spatial channel dispersion. Interestingly, a certain small temporal broadening already occurs for the LOS paths, which is due to the impact of the IFFT and the channel frequency dispersion [18]. On the other hand, the k-factor and σ_{AoA} cannot be defined reasonably for just one path. High delay spreads between 1.99 ns and 3.72 ns as well as angular spreads of up to 40° are determined under consideration of all rays. Without effective spatial filtering, strong intersymbol interference would result in a practical THz communication system. Similar to the k-factor, τ_{RMS} and σ_{AoA} level off from the third reflection order onwards. In consequence, up to second order reflections prove sufficient to model THz propagation channels.

E. Polarization

Polarization exhibits a strong impact on the multipath propagation and the broadband channel characteristics. Now, the ray amplitudes are considered in detail. Fig. 8 illustrates the ray path loss differences at TX$_1$ between linear ϕ and θ polarization. The bars have been sorted by magnitude according to reflection order. Both polarizations have been normalized with the same LOS reference measurement. Note that in total 8 third and fourth order paths could be detected less in horizontal compared to vertical polarization (cf. Table 2) and could hence not be included in Fig. 8.

Occurring additional attenuations due to TM instead of TE reflections range between -1 and 8 dB for once reflected and between -1.8 and 24 dB for twice reflected rays. Negative values are not expected and are just a consequence of an imperfect lens positioning as well as slightly different antenna alignments in horizontal compared to the vertical antenna orientation. It can be seen that the attenuation differences tend to increase with each reflection. In consequence, linear ϕ polarization appears favorable compared to θ polarization to suppress multipath propagation. A drawback is the higher loss on the indirect propagation paths, if these must be utilized for a directed NLOS transmission in case of a LOS blockage.

Additionally, measurements are recorded for both cross polarizations. On the LOS path, cross polarization discriminations

$$\mathrm{XPD} = 20 \cdot \log \left(\frac{E_{\mathrm{Co}}}{E_{\mathrm{Cross}}} \right) \qquad (1)$$

of XPD$_\theta$ = 50.1 dB and XPD$_\phi$ = 42.2 dB have been recorded. XPD$_\theta$ refers to the field received in θ co polarization vs. the field transmitted in ϕ and received in θ polarization. XPD$_\phi$ is defined analogously. These figures correspond to the mere depolarization caused by the antennas. Apart from the LOS ray, power in cross polarization could only be detected in the directions of the first order reflections ray 3 and ray 4 (cf. Fig. 3) due to the limited dynamic range. The XPDs amount to XPD$_{\phi,\mathrm{ray}\,3}$ = 42.8 dB and XPD$_{\theta,\mathrm{ray}\,3}$ = 31.3 dB as well as XPD$_{\theta,\mathrm{ray}\,4}$ = 32.4 dB, whereas XPD$_{\phi,\mathrm{ray}\,4}$ could not be recorded. Compared to the LOS reference measurements, involved reflection and scattering processes cause a decrease of the XPD by only about 7 to 11 dB. In conclusion, depolarization can be neglected in THz communication channels as long as the TX and RX are placed in a horizontal plane and the antennas do not induce a significant depolarization themselves. If the TX and RX are positioned in a plane oblique relative to the walls or reflecting objects, a strong geometric depolarization can be expected [26].

F. MIMO Channels

THz communication systems will most likely employ multi antenna systems because the high propagation loss has to be
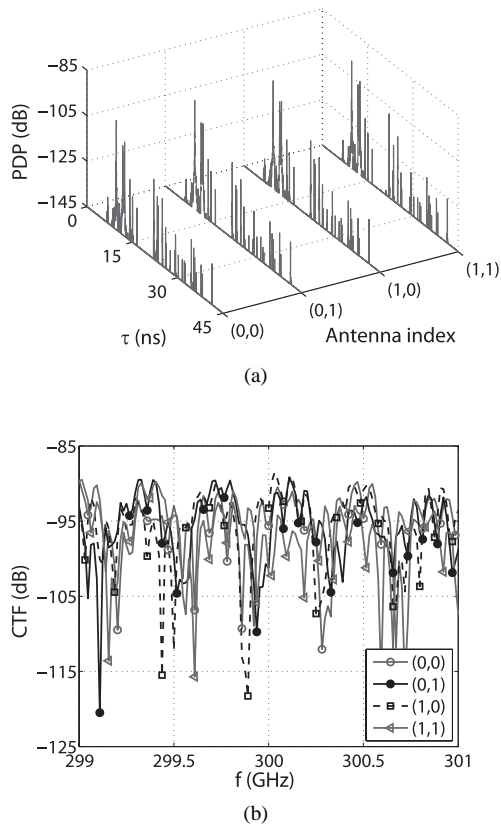
Fig. 9. Measured MIMO PDPs and CTFs for TX_1: (a) PDPs and (b) cut-out of the CTFs.

Fig. 10. 3D model of the measured and simulated scenario including up to second order ray paths.

overcome and the antennas will have to counteract potential ray shadowing [1]. With the aim of investigating the potential of such multi antenna systems, a virtual 2×2 MIMO configuration is considered. The TX and RX are shifted by 1 mm in positive y direction for TX_1 (cf. Fig. 2), which is equivalent to a separation of the virtual MIMO array elements by one wavelength at 300 GHz.

Fig. 9 illustrates the composed recorded power delay profiles. The antenna indices denote the positions of the TX and RX, *i.e.*, (0,0) means the position TX_1, (0,1) means the RX being moved 1 mm in positive y direction *etc*. Very similar, but not identical PDPs are observed for the four antenna constellations. Between the LOS attenuations, a maximum deviation of 0.9 dB occurs, which can be attributed to the general measurement uncertainties like positioning inaccuracies. Similar differences in the order of 1 dB are observed for the reflections. The phase conditions vary entirely for all paths due to the fact that the element spacing of 1 mm already corresponds to a phase shift of 2π. In consequence, the fading behavior of the channels changes, which can be seen using the example of a cut-out of the corresponding CTFs in Fig. 9(b). Only the overall curve shapes, the depths of the fading dips and the distances between two dips qualitatively remain similar regardless of the position.

A measure for the similarity of the CTFs, which also indicates potential channel capacities, is provided by the cross correlation coefficient. Values between 0.6 and 0.86 have been determined for the recorded MIMO CTFs. These indicate a rather high channel correlation, which can also be expected in face of
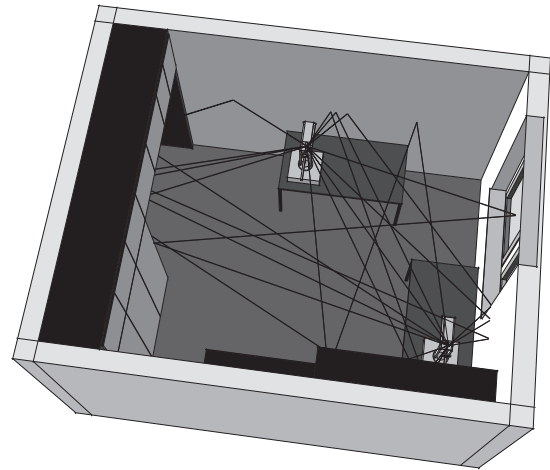
the small element spacings with respect to the large room dimensions. The ergodic MIMO channel capacity [27]

$$C = \log_2 \left| \mathbf{I}_N + \frac{\mathbf{SNR}}{M} \cdot \mathbf{HH}^* \right| \qquad (2)$$

is considered as a simple figure of merit for a performance estimate of a THz MIMO system. M and N are the numbers of transmit and receive antennas, I_N is an identity matrix with the dimensions $N \times N$ and SNR is the signal-to-noise ratio at the RX. Here, the channel matrix $\mathbf{H}$ becomes frequency-dependent in face of the huge employed bandwidth. Therefore, the realistic upper bounds for the ergodic capacity of the broadband channel is obtained by evaluating (2) at each frequency point individually and averaging the results [27]. This corresponds to a transmission with a hypothetical OFDM system, whereas the number of subcarriers equals the number of measurement points [28].

Under the assumption of 10 dB SNR, the theoretical Shannon capacity of a single antenna system amounts to 3.46 bit/s/Hz, whereas the 2×2 MIMO capacity determined from the measurements reaches 6.21 bit/s/Hz. Note that the measured channel is just a snapshot and does not represent a general MIMO capacity, which can only be given in terms of outage probabilities [27] for a large amount of channel realizations.

Spatial multiplexing could obviously yield a performance gain in THz indoor channels. However, sufficient SNRs can in practice not be achieved with omnidirectional antenna elements. Instead, alternative concepts such as distributed antenna setups, receive diversity or antenna arrays with directive elements will have to be investigated in the future. An appropriate propagation model will be required to generate a large set of channel realizations for such studies, which is introduced in the following section.

III. RAY TRACING PROPAGATION MODELING

Deterministic RT propagation modeling has become state of the art for the channel simulation of wireless communication systems. RT will serve to simulate the wave propagation in the

scenario investigated experimentally up to now. Fig. 10 exemplifies ray tracing results for TX_1.

Frequency domain ray tracing is introduced subsequently first. Then, the material parameters are calibrated. Last, the RT simulations are validated with the channel measurements.

A. Frequency Domain Ray Tracing

In contrast to conventional WLANs, huge bandwidths of 10 GHz and beyond require the broadband simulation of THz propagation channels at multiple frequency points [18]. Here, this is done with an in-house developed ray tracing tool in frequency domain. As a basis, the geometric ray search engine from the first part of the paper is adopted to determine the spatial and temporal ray characteristics. Apart from the LOS path and the reflections, also diffusely scattered rays can be respected according to the Kirchhoff theory [12]. However, as the previous section has revealed that no scattered rays could be detected (cf. for instance the PDP at TX_1 in Fig. 5(b)), diffuse scattering is neglected. Diffraction is disregarded also. Transmission through walls, windows or objects does not play any role either in face of very high absorption coefficients [13].

The results of the geometric computations are fed into the electromagnetic engine. The main advantage of separating the geometric from the electromagnetic ray tracing engine is that the very time-consuming geometric calculations have to be performed only once. Output is the electric field strength $E_j(f_i)$ of the jth path for all N_{Rays} rays at one discrete frequency f_i. The calculations are based on the Friis formula, the Fresnel equations and the Rayleigh roughness factor, for what dielectric parameters of all materials are needed. Fully polarimetric channel information is included [26]. Please refer to [18] for details. All electromagnetic evaluations are repeated for N_f frequencies. N_f can be understood analog to the measurement points of a VNA and must be chosen high enough to resolve the maximum expected excess delay.

From the field strengths, the sampled path-specific CTF of the jth ray

$$H_j(f) = \sum_{i=1}^{N_f} E_j(f_i) \cdot \delta(f - f_i) \qquad (3)$$

is composed. After weighting the CTF with the antenna characteristic g

$$H_j'(f) = \sum_{i=1}^{N_f} H_j(f) \cdot g(f, \phi_j, \theta_j), \qquad (4)$$

the complete CTF is computed as

$$H(f) = \sum_{j=1}^{N_{\text{Rays}}} H_j'(f). \qquad (5)$$

Finally, the CIR can be determined from the CTF by performing an IFFT. Note that the equations implicitly respect polarization characteristics of the rays and antennas [26].

B. Calibration

The accuracy of ray tracing simulations strongly depends on the scenario material parameters. These can most likely not be determined isolatedly as probes of walls or reflecting objects may not be available. Moreover, scenario-specific parameters may differ significantly from values in literature. Calibration of the RT simulations with channel measurements still provides an excellent means to improve the prediction precision of the ray tracing tool, even if the material parameters are known only roughly [29]. At the same time, a complete material parameter set is obtained for further RT simulations.

In our previous work [18], an advanced calibration algorithm based on iterative simulated annealing [30] has been developed and tested with measurements, which will now be applied to the measurements from the previous section. As a novelty, the algorithm exploits the spatial and temporal channel information in order to unambiguously map all rays between measurements and ray tracing simulations. Compared to conventional approaches, where the mere difference between the simulated and measured power delay profiles is optimized in most cases, the proposed ray mapping allows for a significant improvement of the calibration results.

The optimization criterion is to minimize the individual deviations between the measured and the simulated ray powers $P_{j,\text{meas}}$ and $P_{j,\text{RT}}$ according to the cost function

$$f(\mathbf{X}) = \sqrt{\frac{\sum_{j=1}^{N_{\text{Rays}}} (P_{j,\text{meas}} - P_{j,\text{RT}})^2}{N_{\text{Rays}}}}. \qquad (6)$$

In each iteration cycle, new material parameters are randomized based on the old parameter set [18], for which the new ray tracing solution $\mathbf{X}$ is computed. Better solutions are always adopted, whereas worse solutions are only accepted with a certain small probability. Unrealistic values with $\varepsilon_r < 1$ are discarded. For increasing cycle numbers, the parameters are varied increasingly less, so that a reliable convergence is achieved after several 10 cycles. As the second main feature, the algorithm is combined with frequency domain ray tracing, so that even frequency-dispersive materials can be calibrated. This is done by splitting the band of interest into multiple subbands and introducing multiple complex ε_r per material, one for each subband. These ε_r are varied independently during the calibration process. Here, 20 different ε_r are allowed for each material over the 50 GHz bandwidth to account for dispersion. Please refer to [18] for further details.

Compared to the previous work, where only one TX/RX position has been taken into account, multiple measurement points are considered for the calibration now. The ray power differences at TX_1, TX_1 in ϕ polarization, and TX_2 are included simultaneously in the cost function (6). Because of the additional information, better and more robust calibration results can be expected compared to just one TX/RX constellation. TX_3 is left out here and will be used for the test of the calibration results later. Due to the fact that only few fourth order rays have been measured and that they are negligible with regard to the overall channel characteristics, only rays up to the third order are respected.

An initial material parameter set is adopted from our previous work [31]. Starting from values of 19.9 dB, 24.7 dB, and 22.6 dB, the cost function definitions with TX_1 only, with TX_1 and TX_2 as well as with TX_1, $TX_{1,\phi \text{ Pol.}}$, and TX_2 converge to
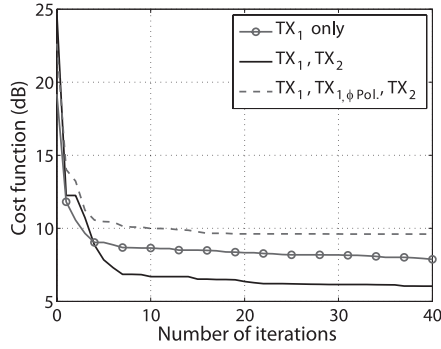
Fig. 11.   Cost function convergence.

Table 5.   Material parameters obtained from the best out of 20 calibration runs.

	Wood (wardrobes)		Plaster (walls)		Glass (windows)	
	ε_r'	ε_r''	ε_r'	ε_r''	ε_r'	ε_r''
Before cal.	1.56	0.41	1.61	0.25	7	1.4
TX_1 only	1.02	1.30	5.75	6.70	4.48	1.25
TX_1, TX_2	1.01	1.65	4.43	8.83	9.14	0.34
TX_1,$TX_{1,\phi\,Pol.}$,TX_2	1.01	1.47	3.73	7.44	8.09	0.85

solutions with minimum cost values of 7.9 dB, 6 dB, and 9.6 dB after 40 iterations. These results have been selected as the best out of 20 calibration runs. The cost function progress can be seen in Fig. 11. Additionally, the material parameters obtained under the assumption of constant material properties over the band are summarized in Table 5. Due to the lack of roughness information about the plaster, a realistic surface height standard deviation of 0.13 mm has been assumed [32]. This property is accounted for in the ray tracing algorithm via the Rayleigh roughness factor. From the material parameter differences between before and after the calibration, the initial plaster characteristics prove least appropriate and are subject to corrections. However, as the actual wall consistency cannot be known, the parameters can be considered to remain within a realistic range. This holds the more for the windows and the wardrobes.

The highest accuracy is achieved with TX_1 and TX_2, whereas the additional introduction of the second linear polarization leads to worse cost values. Reason for this is that ε_r have to be found that match the measurements in both polarizations for TX_1 at the same time. The measurements in the two polarizations are subject to slight independent errors such as imperfect lens placement (cf. Subsection II-E). Due to the fact that the overall cost function is minimized, a compromise between the deviations in the two polarizations is obtained. Generally speaking, the more information is respected, the more universal the results become opposite to potentially higher cost values.

Fig. 12 contrasts a cut-out of the power delay profile for TX_1 before and after calibration. The complete cost function definition with TX_1 in both polarizations and with TX_2 is employed. A significant improvement compared to uncalibrated RT is achieved regardless of the reflection order. Measured and simulated rays deviate by up to 18.2 dB in the depicted temporal range before calibration, which is reduced to a maximum
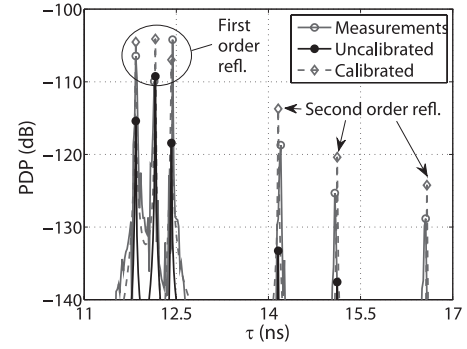
Fig. 12.   Cut-out of the measured, the uncalibrated and the calibrated PDPs at TX_1.
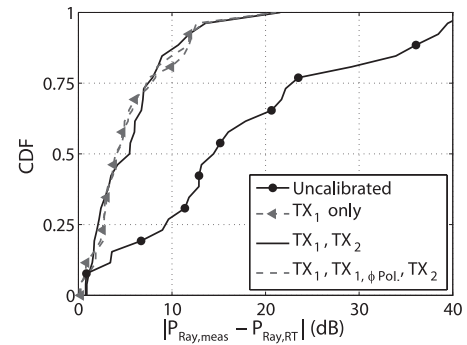
Fig. 13.   Ray power differences between measurements and RT before and after calibration at TX_1.

of 6 dB thereafter.

A quantitative comparison of all ray amplitude deviations at TX_1 is given in Fig. 13. After calibration, 50% of the rays differ by about 5 dB or less, whereas more than 80% of all rays have a deviation of less than 10 dB. Uncalibrated, these figures amount to 14.4 dB and 29 dB, respectively. Note that the power differences are calculated per path. Errors accumulate in case of multiple reflections. The very high deviations of 30 dB and more actually correspond to values in the order of 10 dB per reflection. Remarkably, the cost function definition does not have any significant impact on the high calibration quality. The reason is that the measurements at the different positions implicitly include the same information on the material behavior. Calibration with just one TX obviously already achieves very good results, which agree well with the channels measured for further TX placements. Otherwise, higher cost values would be expected for the cost function definition with TX_1 and TX_2 compared to TX_1 only. Note that this indicates a good and reproducible measurement accuracy, but the deviations still reveal limitations of the possible measurement and calibration precision at THz frequencies.

In order to ensure the universality of the results, the calibrated ray tracing simulations must be tested against further measurements that have not been included in the calibration process. Moreover, measured channel characteristics have to be reproduced correctly, which will be tested in the next Subsection.
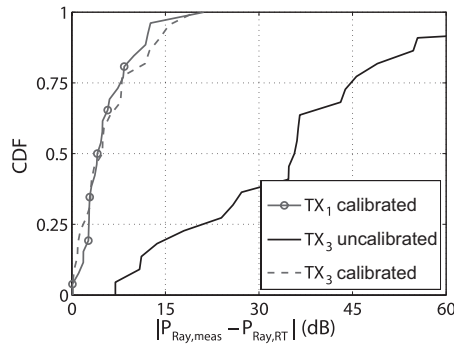
Fig. 14. Difference between measurements and RT simulations at TX position 3 for a cost function respecting TX_1, $TX_{1,\phi Pol.}$, and TX_2.

Table 6. Measured vs. simulated broadband channel characteristics; τ_{RMS} in (ns), σ_{AoD} in (°).

	TX_1		TX_1, ϕ pol.		TX_2		TX_3	
	Mea.	RT	Mea.	RT	Mea.	RT	Mea.	RT
k	1.53	2.76	4.33	3.39	1.85	2.47	4.32	2.97
τ_{RMS}	3.72	4.87	3.55	4.57	1.99	1.63	3.01	5.02
σ_{AoD}	37.0	29.3	24.7	30.9	18.3	22.2	31.7	34.0

C. Comparison between Measurements and RT Simulations

Now, the parameter set obtained after the calibration with TX_1 and TX_2 is adopted for RT predictions at TX_3. Thus, the general applicability of the calibration results to further positions is validated.

Analogously to Fig. 13, Fig. 14 depicts CDFs of the ray amplitude differences between measurements and simulations at TX_3. Here, *calibrated* refers to the RT results with material parameters obtained from the calibration without TX_3. The calibration helps to significantly improve the RT predictions, although TX_3 has *not* been respected in the cost function. Even the amplitude differences at TX_1, serving as reference, are only slightly better than the ones of TX_3. In consequence, the calibration results from just a few points can be used for the accurate wave propagation simulation at further positions.

Allowing for a quantitative evaluation of the ray tracing accuracy, a comparison of the measured and simulated k-factors, the RMS delay spreads and the AoD angular spreads σ_{AoD} is given in Table 6. Similar k-factors result with average deviations around 1, whereas τ_{RMS} is overestimated by 1–2 ns apart from TX_2. σ_{AoD} is in good agreement for $TX_{1,\phi Pol.}$ as well as for TX_2 and deviates by at maximum 7.7° for TX_1. The reasons for the deviations are the residual ray power differences after calibration as well as different LOS attenuations, which cannot be calibrated. Still, compared to the results before calibration, an accuracy improvement is achieved also in terms of the figures of merit. E.g., values of $k = 12.98$, $\tau_{RMS} = 0.90$ ns and $\sigma_{AoD} = 8.9°$ are determined from uncalibrated RT for TX_2, which deviate significantly more from the measurements than after calibration (cf. Table 6). Generally, the overall behavior of the broadband channel properties can be described well with RT. Of course, RT does not reproduce the measurements *exactly*, but still provides a realistic basis for system simulations and the derivation of a first THz channel model. This will be subject to future work.

Regarding the universal reusability of the calibration results, the obtained parameters can of course be employed for RT simulations in other setups given that the same materials are present in the respective scenario. Although the calibration process exploits the spatial channel information for the ray mapping, the calibration outcome does not inherently depend upon the scenario dimensions or shape. The material information is extracted independently from any geometry. New measurements and a recalibration will just be required for other materials.

In order to finally assess the applicability of RT to MIMO channels, channel transfer functions have been generated for the MIMO configuration in Subsection II-F. From the measurements, a channel capacity of 6.21 bit/s/Hz has been calculated, whereas the capacity determined from ray tracing amounts to 5.67 bit/s/Hz. Qualitatively, the simulated and measured capacities agree sufficiently well. Deviations can be explained with the scenario model inaccuracies and with the inherent limitations of the measurements, such as the non-perfect antenna pointing. These slight non-deterministic errors cannot be reproduced by RT and cause a lower spatial correlation in the measurements than in the simulations.

In summary, calibrated frequency domain ray tracing provides a good means to accurately model THz indoor communication channels.

IV. CONCLUSION

In view of future ultra broadband THz communication systems, 50 GHz wide channel transfer functions have been recorded between 275 and 325 GHz in a typical office scenario. Three different transmitter/receiver constellations have been considered, whereas one setup has been measured fully polarimetric. Moreover, a 2×2 MIMO link has been measured with a capacity of 6.21 bit/s/Hz. Up to fourth order reflections could be detected. High measurement accuracies with average ToA and AoA/AoD deviations below 0.2 ns and 2° have been achieved in respect to geometrical considerations. Only up to second order rays noticeably influence the broadband channel properties. Typical attenuations per reflection amount to 12-15 dB.

Additionally, frequency domain ray tracing has been introduced. After calibration with an advanced simulated annealing algorithm, the RT prediction accuracy has been improved significantly. Only a few measured TX positions have already proven sufficient to reach a stable calibration result. Finally, RT has been validated against the measurements. Frequency domain RT has been demonstrated to be well suited to simulate the indoor wave propagation at THz frequencies.

ACKNOWLEDGMENT

REFERENCES

[1] R. Piesiewicz, T. Kleine-Ostmann, N. Krumbholz, D. Mittleman, M. Koch, J. Schoebel, and T. Kürner, "Short-range ultra-broadband terahertz communications: Concepts and perspectives," *IEEE Trans. Antennas Propag. Mag.*, vol. 49, no. 6, pp. 24–39, 2007.

[2] S. Cherry, "Edholm's law of bandwidth," *IEEE Spectr.*, vol. 41, no. 7, pp. 58–60, 2004.

[3] T. Kleine-Ostmann and T. Nagatsuma, "A review on terahertz communications research," *J. Infrared, Millimeter and Terahertz Waves*, vol. 32, no. 2, pp. 143–171, 2011.

[4] H. Song and T. Nagatsuma, "Present and future of terahertz communications," *IEEE Trans. Terahertz Sci. Technol.*, vol. 1, pp. 256–263, Sept. 2011.

[5] M. Tonouchi, "Cutting-edge terahertz technology," *Nature Photon.*, vol. 1, no. 2, pp. 97–105, 2007.

[6] I. Kallfass, J. Antes, T. Schneider, F. Kurz, D. Lopez-Diaz, S. Diebold, H. Massler, A. Leuther, and A. Tessmann, "All active MMIC-based wireless communication at 220 GHz," *IEEE Trans. Terahertz Sci. Technol.*, vol. 1, pp. 477–487, Nov. 2011.

[7] T. Nagatsuma, H. Song, Y. Fujimoto, K. Miyake, A. Hirata, K. Ajito, A. Wakatsuki, T. Furuta, N. Kukutsu, and Y. Kado, "Giga-bit wireless link using 300–400 GHz bands," in *Proc. MWP*, 5 pages (electronic), Valencia, Oct. 2009.

[8] W. Deal, X. Mei, K. Leong, V. Radisic, S. Sarkozy, and R. Lai, "THz monolithic integrated circuits using InP high electron mobility transistors," *IEEE Trans. Terahertz Sci. Technol.*, vol. 1, pp. 25–32, Sept. 2011.

[9] Apr. 2012. [Online]. Available: http://www.ieee802.org/15/pub/IGthz.html

[10] M. W. Chia, B. Luo, and C. K. Ang, "Extremely wideband multipath propagation channel from 285 to 325 GHz for a typical desktop environment," in *Proc. IRMMW-THz*, 1 page (electronic), Rome, Sept. 2010.

[11] S. Priebe, C. Jastrow, M. Jacob, T. Kleine-Ostmann, T. Schrader, and T. Kürner, "Channel and propagation measurements at 300 GHz," *IEEE Trans. Antennas Propag.*, vol. 59, no. 5, pp. 1688–1698, 2011.

[12] C. Jansen, S. Priebe, C. Möller, M. Jacob, H. Dierke, M. Koch, and T. Kürner, "Diffuse scattering from rough surfaces in THz communication channels," *IEEE Trans. Terahertz Sci. and Technol.*, vol. 2, no. 1, pp. 462–472, 2011.

[13] R. Piesiewicz, C. Jansen, S. Wietzke, D. Mittleman, M. Koch, and T. Kürner, "Properties of building and plastic materials in the THz range," *J. Infrared and Millimeter Waves*, vol. 28, no. 5, pp. 363–371, 2007.

[14] C. Jansen, R. Piesiewicz, D. Mittleman, T. Kürner, and M. Koch, "The impact of reflections from stratified building materials on the wave propagation in future indoor terahertz communication systems," *IEEE Trans. Antennas Propag.*, vol. 56, no. 5, pp. 1413–1419, 2008.

[15] W. Malik, D. Edwards, and C. Stevens, "Frequency-dependent pathloss in the ultrawideband indoor channel," in *Proc. IEEE ICC*, vol. 12, Istanbul, pp. 5546–5551, June 2006.

[16] A. Glassner, *An Introduction to Ray Tracing*. Morgan Kaufmann, 1989.

[17] C. Yang, B. Wu, and C. Ko, "A ray-tracing method for modeling indoor wave propagation and penetration," *IEEE Trans Antennas Propag*, vol. 46, no. 6, pp. 907–919, 1998.

[18] S. Priebe, M. Jacob, and T. Kürner, "Calibrated broadband ray tracing for the simulation of wave propagation in mm and sub-mm wave indoor propagation channels," in *Proc. EW*, 10 pages (electronic), Poznań, Apr. 2012.

[19] ITU, *Radio Regulations*. 2008.

[20] T. Schrader, K. Kuhlmann, R. Dickhoff, J. Dittmer, and M. Hiebel, "Verification of scattering parameter measurements in waveguides up to 325 GHz including highly-reflective devices," *Advances in Radio Sci. (Kleinheubacher Berichte)*, vol. 9, pp. 9–17, 2011.

[21] C. Balanis, *Antenna Theory: Analysis and Design*. Harper & Row New York, 1982.

[22] S. Priebe, M. Jacob, and T. Kürner, "The impact of antenna directivities on THz indoor channel characteristics," in *Proc. EuCAP*, 5 pages (electronic), Prague, Mar. 2012.

[23] S. Priebe, M. Jacob, and T. Kürner, "AoA, AoD, and ToA characteristics of scattered multipath clusters for THz indoor channel modeling," in *Proc. EW*, 9 pages (electronic), Vienna, Apr. 2011.

[24] M. Lawton and J. McGeehan, "The application of a deterministic ray launching algorithm for the prediction of radio channel characteristics in small-cell environments," *IEEE Trans. Veh. Technol.*, vol. 43, no. 4, pp. 955–969, 1994.

[25] M. Jacob, S. Priebe, R. Dickhoff, T. Kleine-Ostmann, T. Schrader, and T. Kürner, "Diffraction in mm and sub-mm wave indoor propagation channels," *IEEE Trans. Microw. Theory Tech.*, vol. 60, no. 3, pp. 833–844, 2012.

[26] S. Priebe, M. Jacob, and T. Kürner, "Polarization investigation of rough surface scattering for THz propagation modeling," in *Proc. EuCAP*, 5 pages (electronic), Rome, Apr. 2011.

[27] C. Oestges and B. Clerckx, *MIMO wireless communications: From real-world propagation to space-time code design*. Academic Press, 2007.

[28] J. Wang, S.-H. Zhu, and L. Wang, "On the channel capacity of MIMO-OFDM systems," in *Proc. ISCIT*, vol. 2, Beijing, pp. 1372–1375, Oct. 2005.

[29] J. Jemai, P. Eggers, G. Pedersen, and T. Kurner, "Calibration of a UWB sub-band channel model using simulated annealing," *IEEE Trans. Antennas Propag.*, vol. 57, pp. 3439–3443, Oct. 2009.

[30] L. Ingber, "Simulated annealing: Practice versus theory," *Math. Comput. Modelling*, vol. 18, no. 11, pp. 29–57, 1993.

[31] S. Priebe, M. Jacob, C. Jastrow, T. Kleine-Ostmann, T. Schrader, and T. Kürner, "A comparison of indoor channel measurements and ray tracing simulations at 300 GHz," in *Proc. IRMMW-THz*, 2 pages (electronic), Rome, Sept. 2010.

[32] R. Piesiewicz, C. Jansen, D. Mittleman, T. Kleine-Ostmann, M. Koch, and T. Kürner, "Scattering analysis for the modeling of THz communication systems," *IEEE Trans. Antennas Propag.*, vol. 55, no. 11, pp. 3002–3009, 2007.

Sebastian Priebe was born in Braunschweig, Germany, in 1985. Mr. Priebe received his Dipl.-Ing. and Dr.-Ing. degree in Electrical Engineering from Technische Universität Braunschweig in 2009 and 2013, respectively. During his studies, he was awarded a scholarship by the Chair of TU Braunschweig as well as by the German National Academic Foundation. In 2010, he joined the Institut für Nachrichtentechnik at Technische Universität Braunschweig, having been working in the field of future THz communication systems since then. From September to December 2011, he was with AT&T, studying interference aspects of active and passive THz systems. For this research visit, Mr. Priebe was awarded a scholarship by the German Academic Exchange Service. In his Ph.D. thesis, Mr. Priebe investigated the propagation mechanisms as well as the indoor radio channel properties at THz frequencies and developed a stochastic THz radio channel model. Apart from his scientific publications in the field of THz communications, Mr. Priebe contributed to the channel model for IEEE 802.11ad 60 GHz WLANs. He received the 2011 URSI Commission F Young Scientist Award as well as the Student Paper Distinction Award of the European Wireless Conference 2012.

Marius Kannicht was born in Haldensleben, former East Germany, in 1984. Mr. Kannicht worked at the Physikalisch-Technische Bundesanstalt in Braunschweig from 2005 to 2008. There, he revised the measurement protocol R76-2 for non-automatic weighing instruments according to new regulations and implemented the programming for an automated load cell measurement setup. In 2008, he enrolled at the Technische Universität Braunschweig in Computer and Communications Engineering. Mr. Kannicht is currently working on his bachelor's thesis, in which he dealing with channel measurements at THz frequencies.

Martin Jacob was born in Bielefeld, Germany, in 1982. He received the Dipl.-Ing. degree in Electrical Engineering from the Technische Universität Braunschweig in 2007. Currently, he is pursuing his Ph.D. as a research assistant with the Institut für Nachrichtentechnik at Technische Universität Braunschweig. He is the author of more than 30 technical journal and conference papers in the field of system and channel modeling for UWB, GPS, mm-wave and THz systems. His current research interest lies in the field of wireless communication systems at frequencies of 60 GHz and above. His work mainly focuses on channel and propagation modeling as well as propagation measurements. He is a contributor to the IEEE 802.11ad 60 GHz WLAN channel model and has been a member of the COST 2100 and IC1004 initiatives. Mr. Jacob received the 2011 URSI Commission B Young Scientist Award.

Thomas Kürner received the Dipl.-Ing. degree in Electrical Engineering from Universität Karlsruhe, Germany, in 1990 and the Dr.-Ing. degree from the same university in 1993. From 1990 to 1994, he was with the Institut für Höchstfrequenztechnik und Elektronik (IHE) at Universität Karlsruhe, working on wave propagation modeling, radio channel characterization and radio network planning. From 1994 to 2003, he was with the radio network planning department at the headquarters of the GSM 1800 and UMTS operator E-Plus Mobilfunk GmbH & Co. KG, Düsseldorf, where he was team manager radio network planning support being responsible for radio network planning tools, algorithms, processes and parameters. Since 2003, he has been a Professor for Mobile Radio Systems at the Institut für Nachrichtentechnik (IfN) at Technische Universität Braunschweig. His fields of activity are propagation, traffic and mobility models for automatic planning of mobile radio networks, car-to-car communications, self-organizing LTE networks, indoor channel characterization for high-speed short-range systems including future terahertz communication systems as well as multipath propagation in GNSS systems. In 2012, he was a guest lecturer at Dublin City University. He has been engaged in several international bodies such as ITU-R SG 3, UMTS Forum, NGMN, IEEE 802 and COST 231/ 273/ 259/ 2100/ IC1004. He has been participant in the European projects FP5-IST-MOMENTUM, FP7-ICT-SOCRATES, FP7-SME-GreenNets and FP7-SEMAFOUR. Currently, he is chairing the IEEE802.15 Interest Group THz and the WG Propagation of the European Association on Antennas and Propagation (EurAAP). He served as Vice-Chair Propagation at the European Conference on Antennas and Propagation (EuCAP) in 2007 and 2009 and has been Associate Editor of IEEE Transactions on Vehicular Technology since 2008.